Modifying the Mixed Layer Eddy Parameterization to Include Frontogenesis Arrest by Boundary Layer Turbulence

ABIGAIL S. BODNER,[a] BAYLOR FOX-KEMPER,[a] LEAH JOHNSON,[b] LUKE P. VAN ROEKEL,[c] JAMES C. MCWILLIAMS,[d] PETER P. SULLIVAN,[e] PAUL S. HALL,[a] AND JIHAI DONG[f,g]

[a] Department of Earth, Environmental and Planetary Sciences, Brown University, Providence, Rhode Island
[b] Applied Physics Laboratory, University of Washington, Seattle, Washington
[c] Theoretical Division, Fluid Dynamics and Solid Mechanics, Los Alamos National Laboratory, Los Alamos, New Mexico
[d] Department of Atmospheric and Oceanic Sciences, University of California, Los Angeles, Los Angeles, California
[e] National Center for Atmospheric Research, Boulder, Colorado
[f] School of Marine Sciences, Nanjing University of Information Science and Technology, Nanjing, Jiangsu, China
[g] Southern Marine Science and Engineering Guangdong Laboratory (Zhuhai), Zhuhai, Guangdong, China

(Manuscript received 17 December 2021, in final form 22 August 2022)

ABSTRACT: Current submesoscale restratification parameterizations, which help set mixed layer depth in global climate models, depend on a simplistic scaling of frontal width shown to be unreliable in several circumstances. Observations and theory indicate that frontogenesis is common, but stable frontal widths arise in the presence of turbulence and instabilities that participate in keeping fronts at the scale observed, the arrested scale. Here we propose a new scaling law for arrested frontal width as a function of turbulent fluxes via the turbulent thermal wind (TTW) balance. A variety of large-eddy simulations (LES) of strain-induced fronts and TTW-induced filaments are used to evaluate this scaling. Frontal width given by boundary layer parameters drawn from observations in the General Ocean Turbulence Model (GOTM) are found qualitatively consistent with the observed range in regions of active submesoscales. The new arrested front scaling is used to modify the mixed layer eddy restratification parameterization commonly used in coarse-resolution climate models. Results in CESM-POP2 reveal the climate model's sensitivity to the parameterization update and changes in model biases. A comprehensive multimodel study is in planning for further testing.

SIGNIFICANCE STATEMENT: The ocean surface plays a major role in the climate system, primarily through exchange in properties, such as in heat and carbon, between the ocean and atmosphere. Accurate model representation of ocean surface processes is crucial for climate simulations, yet they tend to be too small, fast, or complex to be resolved. Significant efforts lie in approximating these small-scale processes using reduced expressions that are solved by the model. This study presents an improved representation of the ocean surface in climate models by capturing some of the synergy that has been missing between the processes that define it. Results encourage further testing across a wider range of models to comprehensively evaluate the effects of this adjustment in climate simulations.

KEYWORDS: Ocean dynamics; Turbulence; Oceanic mixed layer; Ocean models

1. Introduction

General circulation models (GCMs) are limited in their ability to resolve the gordian interactions between the atmosphere, ocean, land, and biology over all relevant time and spatial scales. Hence, they simulate these interactions by directly including as many processes as computational constraints permit, while processes too small, fast, or complex are approximated through parameterizations. Parameterizations are reduced mathematical expressions to capture the dominant impacts, while remaining computationally efficient and complementary with other components of the GCM.

The ocean surface layer is the most turbulent layer in the ocean, driven primarily by winds, waves and buoyancy forcing. The ocean surface layer contains the mixed layer, which can be described broadly as the layer in which temperature, salinity, and other tracers are vertically well mixed. It is the connecting layer with the atmospheric boundary layer, where air–sea fluxes take place, and links the deep, stratified ocean waters with the free atmosphere through vertical mixing and surface ventilation (Fox-Kemper et al. 2022). Furthermore, vertical mixing processes near the ocean surface are critical in transporting tracers and supplying essential nutrients to marine biology, as the euphotic zone where primary productivity occurs is coincident with the surface layer (Taylor and Ferrari 2011; Smith et al. 2016; Mahadevan 2016; Olita et al. 2017; Lévy et al. 2018).

Submesoscales span the range of 0.1–10 km in horizontal scale, 0.01–1 km in vertical scale, and from hours to days in

Supplemental information related to this paper is available at the Journals Online website: https://doi.org/10.1175/JPO-D-21-0297.s1.

Bodner's current affiliation: Courant Institute of Mathematical Sciences, New York University, New York, New York.

Corresponding author: Abigail S. Bodner, abigail.bodner@nyu.edu

DOI: 10.1175/JPO-D-21-0297.1

time evolution, and boundary layer turbulence is on the order of meters in length and from minutes to hours in time (e.g., Grant and Belcher 2009; McWilliams 2016). Therefore, submesoscales and boundary layer turbulence tend to be on scales smaller than the grid used in GCMs, even at the highest possible resolution (Dong et al. 2020, 2021). Accurate representation of these processes is especially important for climate simulations as the mixing-versus-restratification balance near the surface determines the effective mixed layer depth, which is an effective marker of overall climate sensitivity in models (Li et al. 2019; Fox-Kemper et al. 2019; Hall and Fox-Kemper 2021, manuscript submitted to *Geophys. Res. Lett.*).

As turbulence mainly acts to stir and diffuse the fluid (Thorpe 2005), two main parameterization methods emerge to represent these effects in GCMs. The classic boundary layer turbulence closure involves a 1D (vertical) representation of the isotropic, small-scale down-gradient fluxes and nonlocal fluxes,

$$\overline{w'\phi'} = K\frac{\partial\overline{\phi}}{\partial z} + \Gamma, \tag{1}$$

where $\overline{\phi}$ represents any resolved (overbar) variable, $\overline{w'\phi'}$ the vertical fluxes from the covariance of unresolved (prime) variables, K is the eddy diffusivity coefficient, and Γ represents any nonlocal effects (e.g., convective plumes). Since $\overline{\phi}$ is resolved by the model, the effort lies in estimating K and Γ to best represent the vertical mixing processes in the upper ocean, which in the Community Earth System Model (CESM2) used here depend on the turbulent velocity scales u_*, w_* and an enhancement factor $\mathscr{E}(\mathrm{La})$ to account for wave effects arising from the turbulent Langmuir number La (e.g., Large et al. 1994; Li et al. 2019).

Stirring by mesoscale and submesoscale eddies is represented by a bolus velocity $\mathbf{u}^B$ acting as an advection term (Gent and McWilliams 1990; Griffies 1998). These velocities are given by a streamfunction ($\boldsymbol{\Psi}$), representing the mesoscale and submesoscale eddy fluxes produced by the restratifying effect of eddies acting to overturn a front (Fox-Kemper et al. 2008),

$$\underbrace{\overline{w'b'}}_{\text{eddy fluxes}} = \boldsymbol{\Psi}\times\nabla_H\overline{b}, \qquad \underbrace{\mathbf{u}^B}_{\text{bolus velocity}} = \underbrace{\nabla\times\boldsymbol{\Psi}}_{\text{streamfunction}}. \tag{2}$$

The restratification process (i.e., mixed layer shoaling) associated with submesoscales is represented by the mixed layer eddy (MLE) parameterization (Fox-Kemper et al. 2011), which captures the effects of baroclinic mixed layer eddies that form along submesoscale fronts in a weakly stratified background state, that is, the mixed layer (Nurser and Zhang 2000; Boccaletti et al. 2007; Fox-Kemper et al. 2008).

The MLE parameterization is given in the form of an eddy-induced overturning streamfunction, which represents the slumping of the front and release of available potential energy (always positive, i.e., restratifying). The streamfunction produces fluxes and an eddy-induced velocity ($\mathbf{u}^{\mathrm{MLE}}$), which are found by the GCM,

$$\overline{\mathbf{u}'b'} = \boldsymbol{\Psi}_{\mathrm{MLE}}\times\nabla\overline{b}, \quad \mathbf{u}^{\mathrm{MLE}} = \nabla\times\boldsymbol{\Psi}_{\mathrm{MLE}}. \tag{3}$$

Note that the MLE parameterization only intends to provide a vertical flux $\overline{w'b'}$ that is reliable. The lateral flux is adjusted so that an eddy streamfunction form remains consistent. For more accurate lateral fluxes, key distinctions between temperature, salinity, and other tracers suggest that both a streamfunction and a diffusivity are needed and scale in a similar way (Bachman and Fox-Kemper 2013; Bachman et al. 2015).

Fox-Kemper et al. (2008) derive the theory for the MLE parameterization and arrive at the following formula for the MLE streamfunction $\boldsymbol{\Psi}_{\mathrm{MLE}}$,

$$\boldsymbol{\Psi}_{\mathrm{MLE}} = C_e\frac{H^2\nabla_H\overline{b}^z\times\mathbf{z}}{|f|}\mu(z), \tag{4}$$

where H is the mixed layer depth, f the Coriolis parameter, $\nabla_H\overline{b}^z$ is the depth averaged horizontal buoyancy gradient over the mixed layer, $0.06 \le C_e \le 0.08$, $\mu(z)$ is a vertical unit vector, and the vertical structure function is approximated by

$$\mu(z) = \max\left\{0, \left[1-\left(\frac{2z}{H}+1\right)^2\right]\left[1+\frac{5}{21}\left(\frac{2z}{H}+1\right)^2\right]\right\}, \tag{5}$$

which causes the parameterized vertical fluxes to vanish below the mixed layer, that is, when $z < -H$, and as the surface is approached, that is, when $z \to 0$.

Implementing the parameterization in coarse-resolution climate models introduces a factor of $\Delta s/L_f$, found to be proportional to the ratio between the *resolved* buoyancy gradient squared and the *full* buoyancy gradient squared, where Δs is the horizontal grid scale and L_f the frontal width parameter. The $\Delta s/L_f$ factor arises from statistically estimating the average intensity of unresolved fronts in a single grid cell, assuming a submesoscale buoyancy spectral slope of k^{-2} [see Eq. (11) in Fox-Kemper et al. 2011]. It is important to clarify that L_f represents the smallest frontal width of unresolved fronts that appear in a grid cell of size Δs. Thus, the frontal width scale L_f is distinctly different from the mixed layer instability scale whose effects are being parameterized within Δs (see also Callies and Ferrari 2018b). The MLE streamfunction that is implemented in GCMs is given by

$$\boldsymbol{\Psi} = C_e\frac{\Delta s}{L_f}\frac{H^2\nabla_H\overline{b}^z\times\mathbf{z}}{\sqrt{f^2+\tau^{-2}}}\mu(z). \tag{6}$$

The substitution of $f \to \sqrt{f^2+\tau^{-2}}$ is used to renormalize (4) across the equator, with a chosen constant parameter for the mixing time scale of $\tau \approx h/u_*$, where h and u_* are the boundary layer depth and friction velocity (also defined in Table 1).

The parameter for frontal width has traditionally been a constant in some models [e.g., the Modular Ocean Model (MOM)], taken to be in the range 500 m $\le L_f \le$ 5 km, whereas in other models [e.g., Parallel Ocean Program (POP)] it has been taken as

$$L_f = \max\left\{\frac{NH}{|f|}, \frac{\nabla_H\overline{b}^z H}{f^2}, L_{f,\min}\right\}, \tag{7}$$

TABLE 1. Dimensional parameters. Note that we do not need any of the thermal expansion parameters β or g, because they are represented by w_* and N. We are also assuming that Stokes drift is not a different scaling from u_* (i.e., fixed turbulent Langmuir number for fully developed waves). The molecular viscosity ν_m and diffusivity κ_m can be suppressed assuming $\mathrm{Re} = Uh/\nu_r \gg 1$ and $\mathrm{Pe} = w_* h/\kappa_m \gg 1$ (e.g., Bodner and Fox-Kemper 2020).

Vertical momentum flux	$\overline{u'w'}$	Mean horizontal velocity	U
Vertical buoyancy flux	$\overline{w'b'}$	Turbulent friction velocity	$u_* = \sqrt{\tau/\rho}$
Coriolis parameter	f	Turbulent convective velocity	$w_* = (B_0 h)^{1/3}$
Mixing layer depth	h	Brunt–Väisälä frequency	N
Mixed layer depth	H	Frontal width	L_f

where $L_{f,\min}$ is an artificial limiter to ensure stability, and NH/f is the mixed layer deformation radius, which were based on estimates of frontal width suggested by observations and geostrophic frontal adjustment theory (e.g., Tandon and Garrett 1994; Hosegood et al. 2006). Furthermore, stratification is not a robust measurement in most GCMs, and accurately defining N from boundary layer mixing schemes can be difficult (e.g., Li et al. 2019). This is the primary reason for the second formulation in (7), which anticipates the deformation radius after geostrophic adjustment has occurred (i.e., assumes $\mathrm{Ri} = N^2 f^2/|\nabla_H \overline{b}^z|^2 \sim 1$).

However, over the past decade, several studies have shown these assumptions to be overly restrictive on the one hand, as argued by Calvert et al. (2020) that due to a natural cancellation of the NH/f formulation with the other buoyancy gradients in (6) and (3), the cutoff $L_{f,\min}$ is not needed under careful numerical implementation. On other hand, this scaling has been shown to be too simplistic, especially in the presence of surface forcing, such as winds and convection (e.g., Mahadevan et al. 2010; Callies and Ferrari 2018a) or in simulations with initial frontal widths selected far from this value or freely evolving without mesoscale strain (Callies and Ferrari 2018b). This uncertainty highlights the strong dependence of the parameterization (7) on frontal width L_f, for which no mechanistic scaling law currently exists to comprehensively evaluate it, or its relationship to the turbulent processes that help set it.

The process involving the formation and sharpening of fronts is known as frontogenesis (e.g., Hoskins and Bretherton 1972; McWilliams 2021). In the ocean, the mixed layer is weakly stratified in the vertical, thus horizontal density gradients can become dominant, and strengthen to form sharp horizontal fronts. Two primary mechanisms are found to onset frontogenesis: a density gradient in the presence of (i) an external strain field (e.g., mesoscale eddies), and (ii) vertical turbulent fluxes (e.g., boundary layer turbulence).

Classic *strain-induced frontogenesis* theory was originally developed by Hoskins and Bretherton (1972) in a semigeostrophic framework, which assumes geostrophic balance in the alongfront direction, thus reducing to a 2D inviscid, adiabatic flow (i.e., no turbulence) in the cross-frontal plane. Classic frontogenesis theory is able to describe frontal dynamics at leading order, by solving for the alongfront current (at the top and bottom of the mixed layer) and a cross-frontal ageostrophic overturning circulation. However, it results in an infinitely narrow front in a finite time, an unphysical limit that does not comply with observations (Hosegood et al. 2006; Ramachandran et al. 2018; Johnson et al. 2020) or numerical simulations (Suzuki et al. 2016; Sullivan and McWilliams 2018). Furthermore, semigeostrophy is found to be inaccurate for 3D flows such as elongated fronts where curvature matters or during late frontogenesis when instabilities develop along the front (Rotunno et al. 1994; Gent et al. 1994).

A different approach combines geostrophic and boundary layer theories, as expected for submesoscale fronts in the ocean surface boundary layer (McWilliams 2016). Here, Ekman and thermal wind are both assumed to be at first order, thus leading to a three-way balance between vertical shear $s(z) = \partial \mathbf{u}_H/\partial z$, the horizontal buoyancy gradient $\nabla_H b(z)$, and turbulent viscosity ν generated by surface winds $\partial^2(\nu \mathbf{s})/\partial z^2$,

$$f\hat{\mathbf{z}} \times \mathbf{s} = -\nabla_H b + \frac{\partial^2(\nu \mathbf{s})}{\partial z^2}. \tag{8}$$

The process of *turbulence-induced frontogenesis* critically involves the turbulent thermal wind (TTW) balance developed by Gula et al. (2014) and McWilliams et al. (2015), also analogous to the generalized Ekman equation (Cronin and Kessler 2009). TTW theory is found to be more consistent with ocean submesoscales, allowing for larger Rossby numbers as fronts and filaments arrive at scales much sharper than described by semigeostrophic theory (McWilliams 2021). However, it is very difficult to observe the strain field and turbulent fluxes in the ocean, and observations of TTW are scarce. Regional ocean models have been useful tools for studying TTW behavior in a near-realistic environment (e.g., Gula et al. 2014; Dauhajre and McWilliams 2018), and only recently have high-resolution numerical simulations been able to simulate the multiscale TTW range. Sullivan and McWilliams (2018, 2019) are among the first to simulate dense filaments undergoing TTW frontogenesis in the presence of realistic surface boundary layer turbulence.

Both strain-induced and turbulence-induced frontogenesis proceed until disrupted by turbulent fluxes that arrest the ever strengthening front (Bodner et al. 2020). It is also possible for strain-induced fronts to be advected out of the frontogenetic confluent strain region and thereby stop frontogenesis before the occurrence of arrest (or singularity). These turbulent fluxes can result from frontal instabilities or ocean surface forcing such as winds, waves, and surface cooling (McWilliams 2021).

There are various instabilities that populate the upper ocean, due to the effects of winds, waves and stratification, that may affect the evolution of fronts: gravitational instability or pure convection (Haine and Marshall 1998); symmetric instability (SI), which mixes along isopycnals in the presence of down-front winds and negative potential vorticity (PV)

(Hoskins 1974; Thomas et al. 2013; Bachman et al. 2017); mixed layer baroclinic instability, which acts to restratify the mixed layer by slumping buoyancy gradients from horizontal to vertical (Boccaletti et al. 2007; McWilliams et al. 2009; McWilliams and Molemaker 2011); Langmuir turbulence, which creates convergence zones at the ocean surface and contributes to upper ocean mixing (McWilliams et al. 1997; Hamlington et al. 2014; Suzuki et al. 2016); horizontal shear instability due to the sharpening front itself (Sullivan and McWilliams 2018, 2019); and other mixing, wave breaking, and topographic effects (Garrett and Loder 1981; Thompson 2000; Teixeira and Belcher 2002; Nagai et al. 2006; Sullivan et al. 2007; Gula et al. 2016). Some of these phenomena require horizontal gradients such as a front to exist (e.g., symmetric instability or baroclinic instability), while others are related more generally to surface forcing (e.g., boundary layer turbulence).

Each of these instabilities may be recognized by characteristic energy sources, scale, and dependence on favorable stratification or shear conditions (Haney et al. 2015). In the ocean, observations are rarely able to simultaneously and conclusively isolate this set of constraints, so novel theoretical and modeling approaches are useful to study these processes and how they interact in a more idealized setting. Submesoscale and boundary layer turbulence can be differentiated by energetic properties (e.g., Hosegood et al. 2006; Haney et al. 2015), lack of hydrostasy (Hamlington et al. 2014) and dynamical markers such as PV (Bodner and Fox-Kemper 2020). Large-eddy simulations (LES) are particularly useful for their study. As computational capabilities have increased in recent years, several studies have modeled the multiscale interactions between submesoscales and boundary layer turbulence.

Skyllingstad and Samelson (2012) studied the interaction between MLE and small-scale turbulence using a nonhydrostatic LES of a warm filament in the presence of Langmuir turbulence, focusing primarily on the transfer of energy between MLE and boundary layer turbulence. Hamlington et al. (2014) studied the weak interaction limit between boundary layer turbulence and submesoscale eddies, and the associated instabilities that arise from this interaction. They compare cases of shear turbulence driven by wind stress, with Langmuir turbulence driven by wind and wave effects. Haney et al. (2015) focus more specifically on how wave effects can alter the PV field and promote certain instabilities along a submesoscale front. Suzuki et al. (2016) identified a strain-induced front in a subdomain from the Hamlington et al. (2014) LES and investigates what energizes and torques the submesoscale front in the presence of waves. Crowe and Taylor (2020) study the evolution of an idealized TTW submesoscale front under varying wind stress and buoyancy flux conditions.

Few studies on interactions between submesoscales and boundary layer turbulence focus on the mechanism of frontogenetic arrest and how it selects stable frontal width. Bodner et al. (2020) propose a theoretical framework for the effects of turbulence on frontal formation in the quasigeostrophic limit. Vertical turbulent fluxes were found to enhance frontogenesis whereas horizontal fluxes are able to oppose it. The tendency and effects of turbulent processes on frontogenesis in Bodner et al. (2020) are consistent with LES studies of frontal evolution (e.g., McWilliams 2017; Sullivan and McWilliams 2018, 2019), where vertical turbulent fluxes assist frontogenesis, and horizontal processes can arrest or contribute to its decay. Note that both vertical and horizontal instabilities on small scales will lead to isotropic 3D turbulence and serve both roles eventually.

These studies have set the scene for a more physical estimate of frontal width, accounting for the interactions between fronts and boundary layer turbulence to determine a scale comparable to that observed. Here we propose and test a new scaling motivated by these principles. In section 2 the new frontal width scaling law is presented that relates L_f to surface forcing parameters. Based on TTW theory, this scaling highlights key balances required for frontogenesis and frontogenetic arrest. Section 3 tests the new scaling in a collection of large-eddy simulations and data from a realistically forced General Ocean Turbulence Model (GOTM) ensemble. Some impacts of the new parameterization as implemented in CESM2 are discussed in section 4. Summary and discussion are given in section 5.

2. A new scaling for frontal width

Following McWilliams et al. (2015), we define the horizontal shear vector as

$$\mathbf{s}(z) = \frac{\partial \mathbf{u}_H}{\partial z} \tag{9}$$

In the TTW balance, thermal wind balance and Ekman balance appear at the same order. Thus, the horizontal buoyancy gradient $\nabla_H b(z)$ balances the shear term together with the (turbulent eddy) viscosity term $\partial^2(\nu \mathbf{s})/\partial z^2$, which is typically generated by surface wind stress τ^s (Fox-Kemper et al. 2022):

$$\nabla_H b = -f\hat{\mathbf{z}} \times \mathbf{s} + \frac{\partial^2(\nu \mathbf{s})}{\partial z^2}. \tag{10}$$

The buoyancy gradient variance equation for $|\nabla_H b|^2$ can be extended from the TTW balance equations. All blended cross terms cancel out with the assumption that the derivatives of $\mathbf{s}$ are aligned with $\mathbf{s}$ (i.e., spiraling can be present but should not set the overall scaling),

$$|\nabla_H b|^2 = |f\hat{\mathbf{z}} \times \mathbf{s}|^2 + \left|\frac{\partial^2(\nu \mathbf{s})}{\partial z^2}\right|^2. \tag{11}$$

We next use scale analysis to explore this equation and the horizontal scale that sets this three-way balance.

The Buckingham Pi theorem helps establish potential relationships among a set of dimensional parameters. The number of dimensional parameters can be reduced by converting most parameters to dimensionless ratios and making appropriate empirical assumptions. A total of 10 dimensional parameters with fundamental dimensions of length and time (Table 1) gives a total of $10 - 2 = 8$ dimensionless

TABLE 2. Dimensionless parameters.

Rossby number	$\mathrm{Ro} \equiv \dfrac{U}{fL_f}$	Richardson number	$\mathrm{Ri} \equiv N^2h^2/U^2$
Turbulent Ekman number	$\mathrm{Ek} \equiv \dfrac{\overline{u'w'}}{hfU}$	Turbulent Prandtl number	$\mathrm{Pr} \equiv \dfrac{hN^2\overline{u'w'}}{U\overline{w'b'}}$
Horizontal velocity ratio	U/u_*	Turbulent velocity ratio	u_*/w_*
Mixing vs mixed layer ratio	h/H	Aspect ratio	h/L_f

parameters (Table 2). The relationship we seek is a function $\mathscr{F}$ in the form

$$0 = \mathscr{F}(\mathrm{Ro}, \mathrm{Ri}, \mathrm{Ek}, \mathrm{Pr}, U/u_*, u_*/w_*, h/H, h/L_f), \tag{12}$$

which is equivalent to a finding the dimensional parameter L_f as a function of all other parameters. Initially, all dimensionless parameters in (12) are considered and under the careful set of assumptions described below we show that L_f emerges as dependent only on a subset of the original parameters. The Buckingham Pi theorem is also a useful framework to consider for any future testing of the parameterization.

In order for frontogenesis to coexist with both submesoscales and the TTW balance, we insist on an MLE-TTW framework: all scaling theories for submesoscales and boundary layer turbulence be consistent at the length scale of the arrested fronts. In the boundary layer, the turbulent convective velocity is defined as

$$w_* = (B_0 h)^{1/3}, \tag{13}$$

where $B_0 = g\beta Q_*$ is the surface buoyancy flux ($B_0 > 0$ for destabilizing conditions), g is gravity acceleration, β the thermal expansion coefficient, and Q_* is the convective surface heat flux. And the turbulent friction (i.e., shear) velocity is defined as

$$u_* = \sqrt{\frac{|\tau_0|}{\rho_0}}, \tag{14}$$

where $\boldsymbol{\tau}_0$ is the wind stress and ρ_0 is a reference density. A general horizontal shear will scale as

$$\frac{\partial \overline{\mathbf{u}}}{\partial z} \sim \frac{U}{h}, \tag{15}$$

where h is the boundary layer depth and U is a generic shear velocity scale, both purposely left unspecified for now. It follows that the shear production scales as

$$\overline{\mathbf{u}'w'}\frac{\partial \overline{\mathbf{u}}}{\partial z} \sim \begin{cases} u_*^2\dfrac{U}{h} & \text{if } w_* = 0, \\ w_*^2\dfrac{U}{h} & \text{if } u_* = 0. \end{cases} \tag{16}$$

In cases forced with both convection and stress, boundary layer mixing schemes such as the K-profile parameterization (KPP; Large et al. 1994) and the energetics-based planetary boundary layer scheme (ePBL; Reichl and Hallberg 2018) tend to use combinations of the convective and friction velocities. A convenient formulation from ePBL's energy budget considerations is $\overline{\mathbf{u}'w'} = (m_* {u_*}^3 + n_* {w_*}^3)^{2/3}$. In Reichl and Hallberg (2018), the dimensionless parameters m_*, n_* are given by specific formulas based on tuning to LES and desired properties of boundary layer turbulence. For simplicity, here we use their approximate average values from Reichl and Hallberg (2018), m_*, $n_* \approx 0.5$, 0.066; however, this analysis can easily be extended to include their space and time dependent values (as calculated in a GCM using ePBL, or equivalently any parameterization for $\overline{\mathbf{u}'w'}$ found in a GCM).

Thus, for an eddy viscosity closure,

$$\overline{\mathbf{u}'w'} = -\nu\frac{\partial \overline{\mathbf{u}}}{\partial z}, \tag{17}$$

and following the definition in the supplemental material and the ePBL scaling, a turbulent Ekman number can be written as

$$\mathrm{Ek} \equiv \frac{\overline{u'w'}}{hfU} \sim \frac{(m_*u_*^3 + n_*w_*^3)^{2/3}}{hfU}. \tag{18}$$

We motivate a choice for the buoyancy anomaly scaling from the vertical stratification assuming that boundary layer turbulence and/or plumes may mix the full depth of the layer, which can be related to the Richardson number as

$$b \sim N^2h = \mathrm{Ri}\frac{U^2}{h}. \tag{19}$$

By setting $\mathbf{s} \sim (U/h)$, $b \sim \mathrm{Ri}(U^2/h)$, and $\nu(\partial\overline{\mathbf{u}}/\partial z) \sim (m_*u_*^3 + n_*w_*^3)^{2/3}$, the TTW buoyancy variance Eq. (11) can now be written as

$$\begin{aligned} |\nabla_H b|^2 &= |f\hat{\mathbf{z}} \times \mathbf{s}|^2 + \left|\frac{\partial^2(\nu\mathbf{s})}{\partial z^2}\right|^2 \\ \rightarrow \mathrm{Ri}^2\frac{U^2}{f^2L_f^2} &= 1 + \frac{(m_*u_*^3 + n_*w_*^3)^{4/3}}{U^2h^2f^2} \end{aligned} \tag{20}$$

Notice that $U^2/f^2L_f^2$ is the frontal-scale Rossby number squared, and the last term on the right-hand side is the Ekman number squared. So Eq. (20) can also be written as

$$\mathrm{Ri}^2\mathrm{Ro}^2 = 1 + \mathrm{Ek}^2. \tag{21}$$

For a three-way balance to hold, the following conditions need to be met,

1) $\mathrm{Ri}^2\mathrm{Ro}^2 = O(1)$,
2) $\mathrm{Ek}^2 = O(1)$, and
3) $\mathrm{Ri}^2\mathrm{Ro}^2/\mathrm{Ek}^2 = O(1)$.

These conditions select for a submesoscale front, where both boundary layer turbulence theory and geostrophic theory balance simultaneously, which together are the essence of TTW theory. In the submesoscale, the Rossby and Richardson numbers are $O(1)$.

However, the first condition requires that the Rossby and Richardson numbers vary inversely together. This can be written as

$$\mathrm{RoRi} = c_1, \tag{22}$$

where c_1 is an $O(1)$ constant. Note that in the original MLE parameterization (7), L_f is scaled by the deformation radius to obey $\mathrm{Bu} = \mathrm{Ro}^2\mathrm{Ri} = 1$, which is not the same scaling as (22).

From the second condition, h emerges as proportional to the Ekman depth, that is, $h \propto \overline{u'w'}/(fU) = (m_* u_*^3 + n_* w_*^3)^{2/3}/(fU)$, or $h = c_2[(m_* u_*^3 + n_* w_*^3)^{2/3}/(fU)]$, where $c_2 = O(1)$.

Expanding the third condition gives

$$\frac{\mathrm{RiRo}}{\mathrm{Ek}} = \frac{1}{c_3} \rightarrow \mathrm{Ri}\frac{U}{fL_f} = \frac{1}{c_3}\frac{(m_* u_*^3 + n_* w_*^3)^{2/3}}{Uhf}$$
$$\rightarrow L_f = c_3 \mathrm{Ri}\frac{U^2}{(m_* u_*^3 + n_* w_*^3)^{2/3}}h, \tag{23}$$

where c_3 is a constant and is $O(1)$.

Thus, for this three-way balance to hold, and eliminating the unspecified scale U, the following scaling for L_f emerges:

$$L_f = C_L \frac{(m_* u_*^3 + n_* w_*^3)^{2/3}}{f^2}\frac{1}{h}, \tag{24}$$

where $C_L = c_2^2 c_3 \mathrm{Ri} \equiv O(\mathrm{Ri})$. For simplicity, the Richardson number will be set to $\mathrm{Ri} = 0.25$, associating the arresting mechanism with shear instability (discussed in more detail in section 3).

In the Buckingham Pi framework this can be written as

$$0 = \mathscr{F}(\mathrm{Ro}, \mathrm{Ri}, \mathrm{Ek}, u_*/w_*, h/L_f). \tag{25}$$

Neither the Prandtl number nor mixed layer depth come up in this thought process of a scaling permitting the three-way TTW balance, and so the frontal width based on that approach is entirely independent of them. Thus (25) is different from (12), which included a potential dependence on H and κ.

Furthermore, as we will be making some assumptions about Ro, Ek, Ri, and their relationships, it may be more intuitive to understand the scaling for frontal width as a relationship among only dimensional parameters,

$$L_f = \mathscr{L}(u_*, w_*, f, h), \tag{26}$$

where we note that the arguments to this function $\mathscr{L}$ are readily available in GCMs.

Including the new scaling for L_f in the MLE streamfunction expression (6) yields

$$\mathbf{\Psi} = C_e \frac{\Delta s}{L_f}\frac{H^2 \nabla \overline{b}^z \times \mathbf{z}}{\sqrt{f^2 + \tau^{-2}}}\mu(z) \Rightarrow C_r \frac{\Delta s |f| h H^2 \nabla \overline{b}^z \times \mathbf{z}}{(m_* u_*^3 + n_* w_*^3)^{2/3}}\mu(z), \tag{27}$$

where $C_r = C_e/C_L$.

This new formula on the right of (27) has a number of immediately apparent advantages over its predecessor on the left. The ad hoc renormalization mixing time scale τ is not needed because the f factors cancel from the denominator. This is an important improvement not only because it eliminates an artificial parameter, but also because the new parameterization naturally vanishes at the equator ($\mathbf{\Psi} \rightarrow 0$ as $f \rightarrow 0$), where the submesoscales become resolved (e.g., Dong et al. 2020). Furthermore, L_f no longer includes a determination of the mixed layer stratification N, which is not robustly extracted from the effects of many boundary layer vertical mixing parameterizations, especially bulk boundary layer formulations (e.g., Kraus and Turner 1967; Price et al. 1986). Interestingly, the cancellation exploited for numerical robustness in the face of uncertain L_f by Calvert et al. (2020) does not occur in this formulation. In the limit where the eddies are given sufficient time to enlarge and their nonlinear scale width grows to exceed the frontal width, the scaling (4) appears to underestimate the restratification rate (Callies and Ferrari 2018b). Including the smaller of the two scales—eddy and front—in the denominator of (27) tends toward reducing this bias, although in this regime the eddy scale is not known (as it is involved in an inverse cascade from initiation at the linear instability scale and thus depends on the unknown time since the onset of instability). In the opposite case, where the front is wider than the instability scale, (27) produces a corrected average frontal strength as argued by Fox-Kemper et al. (2011). It is also important to emphasize that this new formula now involves both the boundary layer depth h and the mixed layer depth H, which are two distinct quantities in climate models. Finally, as was the objective, the surface forcing parameters u_* and w_* play a key role in widening the frontal arrest width by the degree to which turbulence is activated.

3. Proofs of concept

a. Testing in LES

A suite of high-resolution LES are presented and analyzed, where they capture the multiscale character of strain-induced frontogenesis, as it interacts with different instability and mixing mechanisms such as wind forcing and waves, mixed layer instabilities, convection and symmetric instability. In all runs, after instabilities have saturated, the cross-frontal scale halts at a constant width and does not become infinitesimally thin, as theory would predict. Sullivan and McWilliams (2018, 2019) conducted similar experiments for a range of LES, simulating a filament with varying surface forcing conditions. Specifically, they examined the process of frontal formation, arrest and decay of a turbulent-induced (TTW) cold filament in the presence of wind stress, convection and waves. Further

TABLE 3. Estimate of parameterization constants given from strain-induced runs.

	c_1	c_2	c_3
Convection/SI	1.12	6.65	0.13
Stokes and wind	0.64	0.82	1.88
All forcing	2.76	3.38	0.10

details on how these simulations are set up and analyzed can be found in the supplemental material.

We utilize results from these two types of LES (e.g., turbulence-induced and strain-induced frontogenesis) to test the new L_f under various surface forcing conditions (u_*, w_*), the boundary layer depth (h) and the Coriolis parameter (f). For all runs we use the average values for $m_*, n_* = 0.5, 0.066$ from Reichl and Hallberg (2018).

In the turbulent-induced filament frontogenesis cases from Sullivan and McWilliams (2018, 2019, hereafter SM), the parameters used for surface forcing are $u_* = 0.01\,\mathrm{m\,s^{-1}}$ and $w_* = 0.0137\,\mathrm{m\,s^{-1}}$, the Coriolis parameter is $f = 7.81 \times 10^{-5}\,\mathrm{s^{-1}}$ and for each case we use the boundary layer depth found in the supplemental material. To account for the effects of waves, we include the adjustment of $\mathscr{E}u_*$, where $\mathscr{E}$ is the wave-driven turbulence enhancement factor based on Van Roekel et al. (2012), which predicts vertical turbulence fluxes in simulations forced as in SM and is thus appropriate for our TTW based theory (Li and Fox-Kemper 2017),

$$\mathscr{E} = \sqrt{1 + (3.1\mathrm{La})^{-2} + (5.4\mathrm{La})^{-4}}. \qquad (28)$$

Following the SM setup, the coefficients in (28) are those for aligned winds and waves and the Langmuir number is La = 0.32. Note that the enhancement factor is only applied to u_*, as Li and Fox-Kemper (2017) show it does not strongly affect the scaling for fluxes based on w_*.

The set of strain-induced LES runs reported here for the first time were designed to generate fronts that could approach frontogenetic arrest by a number of different mechanisms: influenced by small-scale processes such as mixed layer instabilities (MLI), convection (equivalent to symmetric instability in the presence of a front), wind stress and waves (Stokes drift), all surface forcings combined, and no surface forcing at all. Here, we include the convection/SI, Stokes + wind, and all forcing cases (which also include small MLE). The pure mixed layer instability case and the no forcing case are driven solely by initial conditions and not forced with u_*, w_*, thus they are not configured so as to be able to have the three-way TTW balance and the new frontal width scaling is not applicable. In the Stokes+wind case, $u^* = \sqrt{\tau_0/\rho_0} = 0.001\,\mathrm{m\,s^{-1}}$ and we apply the enhancement factor $\mathscr{E}u_*$ using the Langmuir number $\mathrm{La} = \sqrt{u_*/u_s} = 0.223$ where $u_s = 0.2\ \mathrm{m\ s^{-1}}$. In the convection/SI and all forcing cases, there is penetrating short wave solar radiation in addition to surface cooling. Thus, we use the formula from Eq. (8) of Mironov et al. (2002), which combines penetrating radiation and surface cooling into a single convective velocity scale w_R,

$$w_R = [-(h - \delta)B_R]^{1/3}, \qquad (29)$$

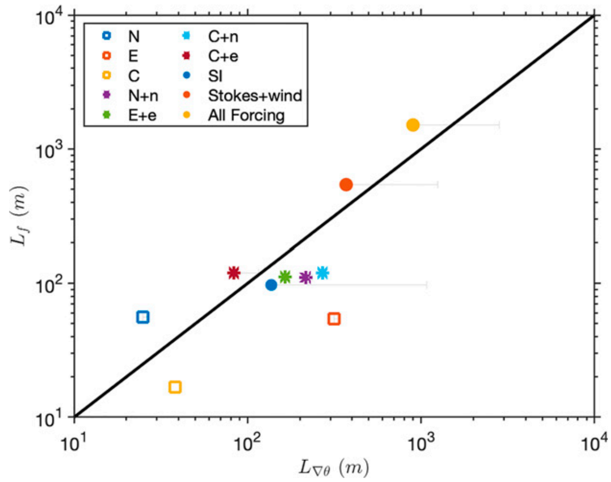

FIG. 1. Log–log plot of the measured $L_{\nabla\theta}^{1\%}$ frontal width compared with the L_f prediction based on the new scaling (24), using the appropriate u_*, w_*, h, and f for each case, and constants set to $m_* = 0.5$, $n_* = 0.066$, and $C_L = 0.25$. Gray error bars represent the measured frontal width given by $L_{\nabla\theta}^{10\%}$. Squares represent the turbulent-induced filament frontogenesis cases from Sullivan and McWilliams (2018), and asterisks represent the same cases including waves from Sullivan and McWilliams (2019); C denotes simulations with surface cooling; N and E denote simulations driven by down-filament and cross-filament winds, respectively; and lowercase n and e denote the same for the direction of surface waves. Circles represent the strain-induced frontogenesis cases: "convection/SI," "Stokes+wind," and "all forcing" (which also include small MLE). Specific parameters are described in section 3a. More details on the individual cases and on the calculation of frontal width can be found in the supplemental material.

where δ is the depth at which the vertical temperature gradient is zero (i.e., maximum), and h is the boundary layer depth.

Horizontal shear instability is found to be associated with frontogenetic arrest, where Ri $\leq$ 0.25 in most strain-induced cases in the supplemental material and as discussed in Sullivan and McWilliams (2018, 2019) and Bodner et al. (2020). Note that it is assumed that the arresting turbulence is isotropic, thus horizontal eddy viscosity is equivalent to vertical eddy viscosity. Hence, we set the Richardson number in the frontal width scaling to match the assumed frontogenetic arrest physics of stratified shear turbulence: Ri = 0.25. Furthermore, as shown in Table 3 the constants c_1, c_2, and c_3 are confirmed by direct diagnosis to be of order 1 in the strain-induced LES. Thus, we choose to set the constant C_L = Ri = 0.25. With a more extensive set of arrested-front LES, this parameter estimate could be improved upon, but each of the LES must span from the shear turbulence scale through to the submesoscale, so they are costly and thus an ensemble of convenience was analyzed to suit the purpose approximately.

Figure 1 is a log–log plot of the measured $L_{\nabla\theta}^{1\%}$ frontal width found in the supplemental material compared with the L_f prediction based on the new scaling (24), using the appropriate u_*, w_*, h, and f for each case, and constants set to $m_* = 0.5$, $n_* = 0.066$, C_L = 0.25. This demonstrates that the new L_f scaling predicts values on the same order of the measured frontal width in all cases. This also implies that even in the strain-induced frontal cases TTW balance holds to some degree. A proper evaluation of the scaling and precise coefficient determination would require a larger suite of costly simulations, varying one parameter at a time over several orders of magnitude. Here the ensemble of convenience serves to demonstrate plausibility over a range of available simulations.

b. Estimates from the GOTM

The latest extension of the GOTM extended to incorporate the CVmix GCM mixing parameterizations (Levy et al. 2014; Li et al. 2021) may be used as a stand-alone model for studying dynamics of boundary layers in natural waters (e.g., Umlauf and Burchard 2005; Li et al. 2019). Here we run GOTM with observed forcing and initialization to provide h, u_*, and w_* by the Cvmix-KPP parameterization, similar to the way it would be computed in a GCM (although without atmospheric coupling or oceanic lateral and vertical transport, e.g., Large et al. 1994; Van Roekel et al. 2018; Li et al. 2019). The frontal width L_f is then predicted based on (24) over four different ocean regimes where submesoscale mixed layer fronts have been shown to be important: the Bay of Bengal (BOB)—June 2018, the site of Air–Sea Interactions in the Northern Indian Ocean (ASIRI) and the Monsoon Intra-Seasonal Oscillations in the Bay of Bengal (MISO-BOB; e.g., Lucas et al. 2016; Ramachandran et al. 2018); the California Current System (CCS) during upwelling—August 2021, the site of Assessing the Effectiveness of Submesoscale Ocean Parameterizations (AESOP) and the current NASA Sub-Mesoscale Ocean Dynamics and Vertical Transport Experiment (S-MODE) campaign for submesoscales (e.g., Capet et al. 2008; Dale et al. 2008; Pallàs-Sanz et al. 2010; Johnson et al. 2020); the Porcupine Abyssal Plain (PAP) in the North Atlantic during winter (January 2021) and spring (May 2021), the site of Ocean Surface Mixing, Ocean Submesoscale Interaction Study (OSMOSIS), Export Processes in the Ocean from Remote Sensing (EXPORTS), and the North Atlantic Bloom (NAB) Experiment (e.g., Thompson et al. 2016).

The histograms corresponding to values of L_f in the four regions are shown in Fig. 2. Although seasonality and monsoon variability will impact this distribution beyond the window of time from the observations, the results are in the range of the submesoscale frontal widths observed, generally $O(1)$ km, with occasionally sharper or wider fronts (e.g., Pallàs-Sanz et al. 2010; Thompson et al. 2016; Ramachandran et al. 2018). Nonetheless, a more quantitative evaluation of the scaling compared with observations is still needed.

c. Evaluations on a global scale

To obtain global statistics of the new L_f scaling we take advantage of the unique configuration from Dong et al. (2020), which uses the recent submesoscale-permitting MITgcm-LLC4320 in tandem with GOTM (see also Rocha et al. 2016; Su et al. 2018). Ocean state variables and surface fluxes (e.g., u_*, w_*) are given at an hourly frequency and used in the offline Cvmix-KPP scheme to determine the boundary layer depth h. Here we also consider

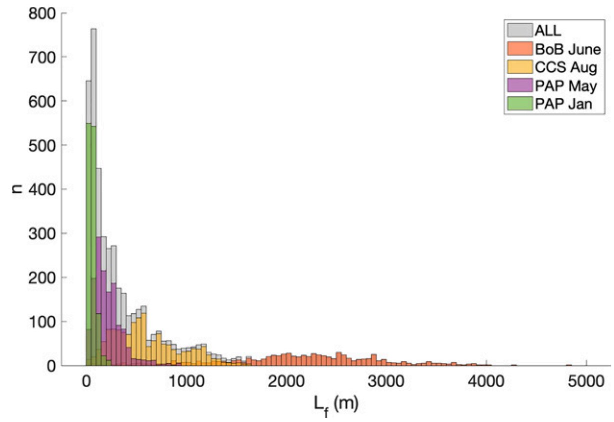

FIG. 2. The L_f (m) estimated from u_*, w_*, and h given by GOTM over four different ocean regimes where submesoscales have been shown to be important: BOB—June 2018; CCS—August 2021; and PAP in the North Atlantic during winter (January 2021) and spring (May 2021).

a correction to u_* due to the turbulent Langmuir number from ECMWF ERA5, which is consistent with the MITgcm-LLC4320 simulation. All constants are identical to the values used in previous sections ($m_* = 0.5$, $n_* = 0.066$, $C_L = 0.25$) and used to calculate L_f from (24). For comparison, the old frontal width scaling based on the deformation radius NH/f is estimated using the mixed layer depth H and buoyancy frequency N given from the Argo data presented in Dong et al. (2020).

Global maps of the old L_f scaling during summer and winter are shown in the upper panels of Fig. 3 and are compared with global maps of the new L_f scaling in the middle panels and zonal median in the bottom panels. The new L_f in Fig. 3 exhibits values ranging from roughly 50 km at the equator to 10 m in the high latitudes, accounting for much sharper fronts than previously obtained by the deformation radius estimate, with a minimum value of only 1 km. This is not to assume that all fronts at high latitudes are 10 m wide, but rather that the contribution of unresolved fronts is given on average from sharper fronts via the k^{-2} spectral slope estimate (Fox-Kemper et al. 2011). In the following section we examine aspects of sensitivity in climate models due to this change in scale factor.

4. Implementation

The new MLE parameterization formula (27) was implemented in the CESM2.1.3-POP model, where the newly required parameters u_*, w_*, and h are all readily available from the surface forcing and the CESM2-standard KPP. We set the constants consistently with the values tested against the LES and GOTM ($m_* = 0.5$, $n_* = 0.066$, $C_L = 0.25$) and all other parameters take the standard values within the existing MLE parameterization scheme (Fox-Kemper et al. 2011). A constraint of $L_{f,\min} = 1$ m was included here to avoid numerical instability in this particular configuration of CESM-POP. As a control case, the old frontal width parameterization (7) was used in otherwise identical simulations with the standard $L_{f,\min} = 5$ km. Thus, to summarize, the MLE parameterization is modified via the

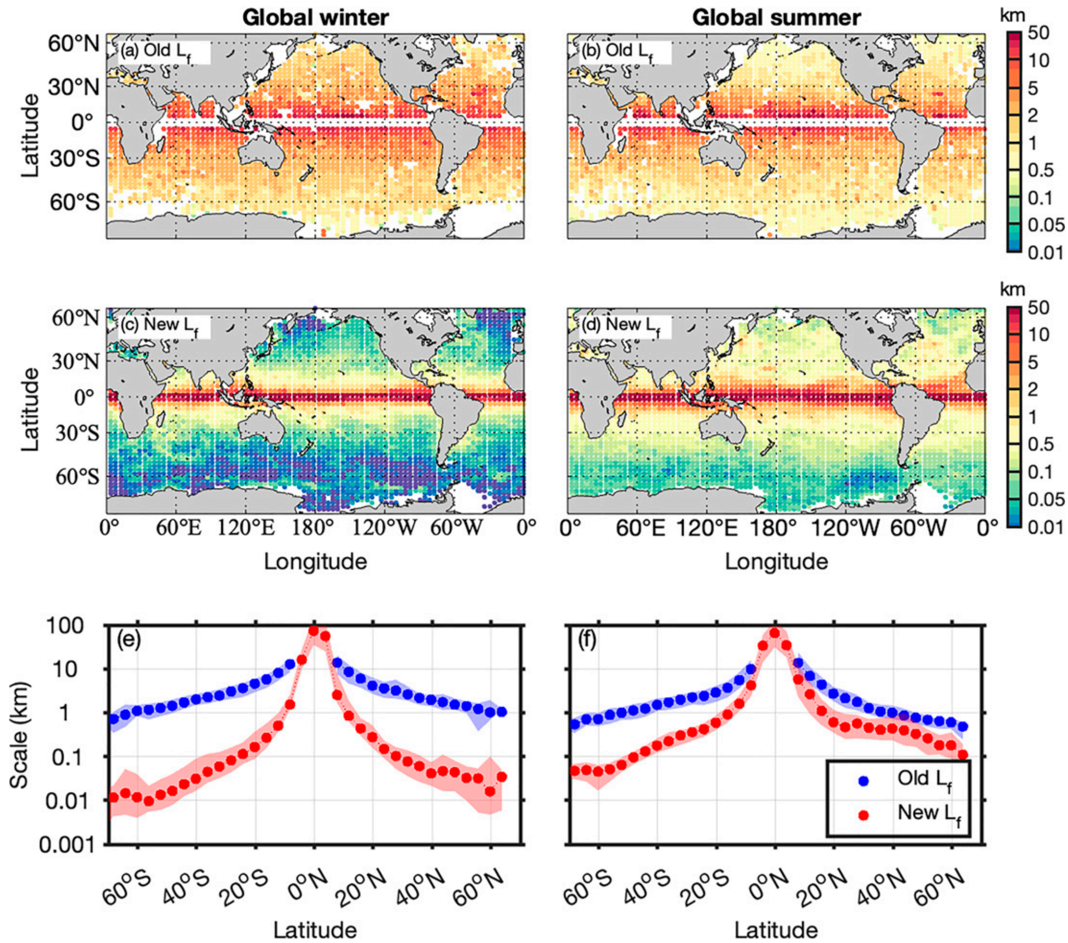

FIG. 3. Global maps of L_f calculated using the (a),(b) old scaling based on the deformation radius NH/f, (c),(d) new scaling based on (24), and (e),(f) their zonal median, with shaded regions denoting the 10th and 90th percentiles. Global winter is given from February and August in the Northern and Southern Hemispheres, respectively, with the opposite during summer. Note that we exclude values of old L_f within 5° of the equator as they become exponentially large.

arrested front width L_f parameter at no additional computational cost to the model.

The new parameterization was tested in two types of simulations: a global fully coupled simulation and a CORE-v2 forced ocean and sea ice simulation, which covers forcing data from 1948 to 2009 (Large and Yeager 2009). The fully coupled model was run for 100 years for both the new and control versions of the MLE parameterizations. The forced model was run for five cycles amounting to a total of 310 simulated years. The mixed layer depth climatology was obtained by averaging over the last 20 years of the coupled simulation and last cycle in the forced simulations.

Figure 4 helps visualize the global values of new L_f across the different CESM simulations. Summer and winter results in both the coupled and forced simulations generally resemble the new L_f values shown in Fig. 3. In particular, the zonal median of new and old L_f shown in Figs. 4e and 4f truly highlight the artificial nature of the old L_f and the imposed $L_{f,\min}$ as compared with the sharper fronts obtained by the new L_f scaling.

Figures 5 and 6 show the mixed layer depth during summer and winter in both hemispheres, respectively, for observations given by the de Boyer Montégut et al. (2004) dataset updated to include Argo data up to 2012, and compared with the control and new parameterization for both the coupled and forced simulations. Most importantly, the results appear to be qualitatively similar in all simulations, and generally resemble observations. This is demonstrated in the top-right panels of Figs. 5 and 6 where scatterplots of the MLD given by new L_f versus control in all simulations and over all grid points are on the same order.

Some sensitivity of the MLD to the new parameterization is apparent and the parts in the world that exhibit these changes are climatically important: for example, the tropical and equatorial summertime regions and near sea ice-covered regions (see observations and discussion in Timmermans and Winsor 2013), such as south of 60°S in austral wintertime where Antarctic Bottom Water forms and the subpolar Atlantic and Greenland and Icelandic Seas. The differences in

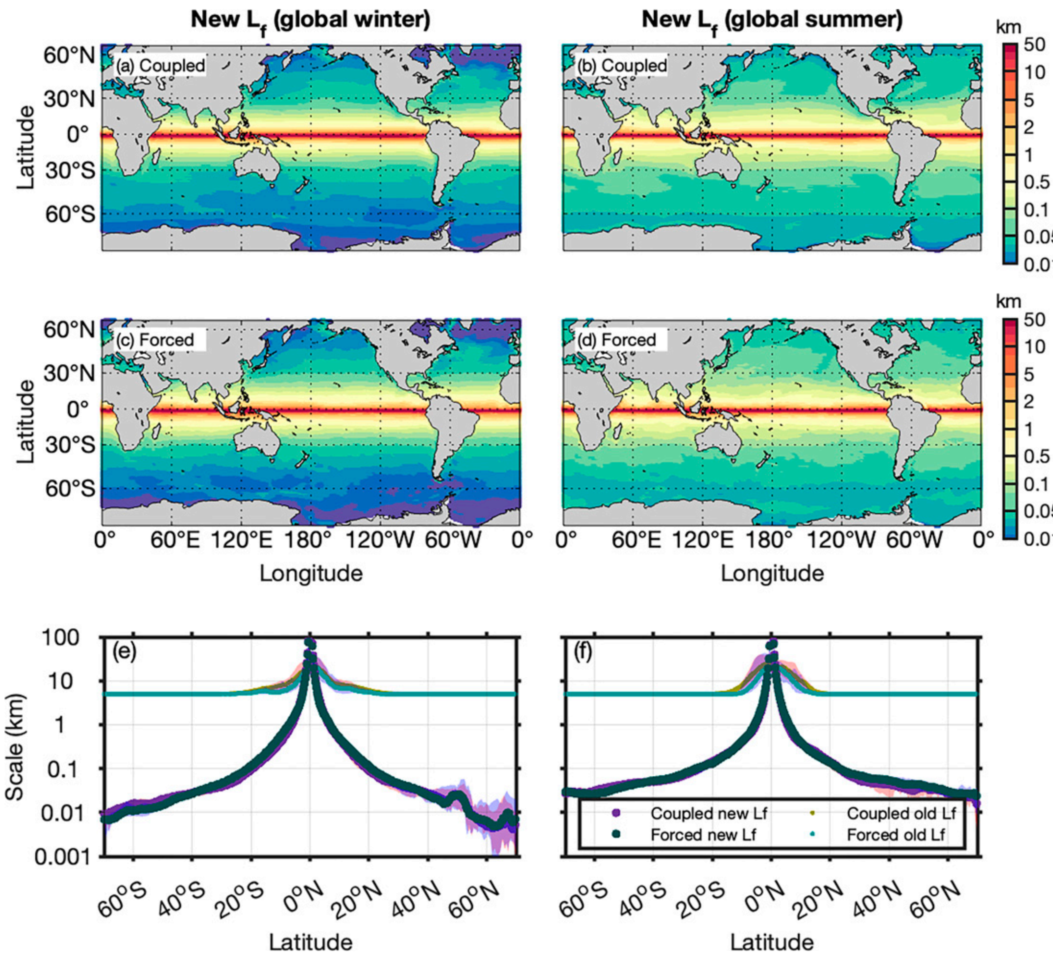

FIG. 4. As in Fig. 3, but for global maps of the new L_f scaling calculated from CESM (a),(b) coupled and (c),(d) forced simulations. (e),(f) Their zonal median is compared with the old L_f based on (7) with $L_{f,\min} = 5$ km (thin lines) used by the control simulations. Here global winter is given from the average of January–March in the Northern Hemisphere and July–September in the Southern Hemisphere, with the opposite during summer.

MLD between the control and new parameterization are highlighted in Figs. 7 and 8 for the coupled and forced simulations, respectively. Multiple panels with custom color bar ranges help identify MLD adjustments on regional scales. These reveal that in the coupled simulations, the new parameterization leads to MLD changes in the North Atlantic, deepening in the Southern Ocean, and shoaling in the equator and Indian Ocean, where reducing the bias has been difficult to achieve by altering boundary layer mixing schemes alone (e.g., Li et al. 2019). Interestingly, although similar global patterns are also apparent in the forced simulations, no significant reduction in the equatorial MLD is visible. The mean reduced bias of the global MLD is given for each season by the average of the $\mathrm{RMSE}_{\mathrm{new}\text{-}L_f} - \mathrm{RMSE}_{\mathrm{control}}$, where RMSE is the root-mean-square error of each case relative to observations. In summer, the MLD bias is reduced by an average of 0.88 and 1.77 m in the coupled and forced simulations, respectively. In winter, when submesoscales are more active, the bias is reduced more significantly by 8.76 and 10.89 m in the coupled and forced simulations, respectively. A detailed multimodel ensemble study with more careful comparison to a wider variety of observations is planned in an upcoming paper.

5. Summary and discussion

Submesoscales and boundary layer turbulence are instrumental in modulating the transfer of heat, momentum, carbon, and other properties between the atmosphere and ocean interior. Accurate representation of these processes in models is crucial, yet they tend to be on scales smaller than the grid used, even at the highest possible resolution. The current MLE parameterization represents the restratification process of adjusting submesoscale fronts, but it has been shown to be too simplistic in circumstances where the frontal width effects are impactful.

Here we propose a new scaling law that relates frontal width with boundary layer turbulence by building on the

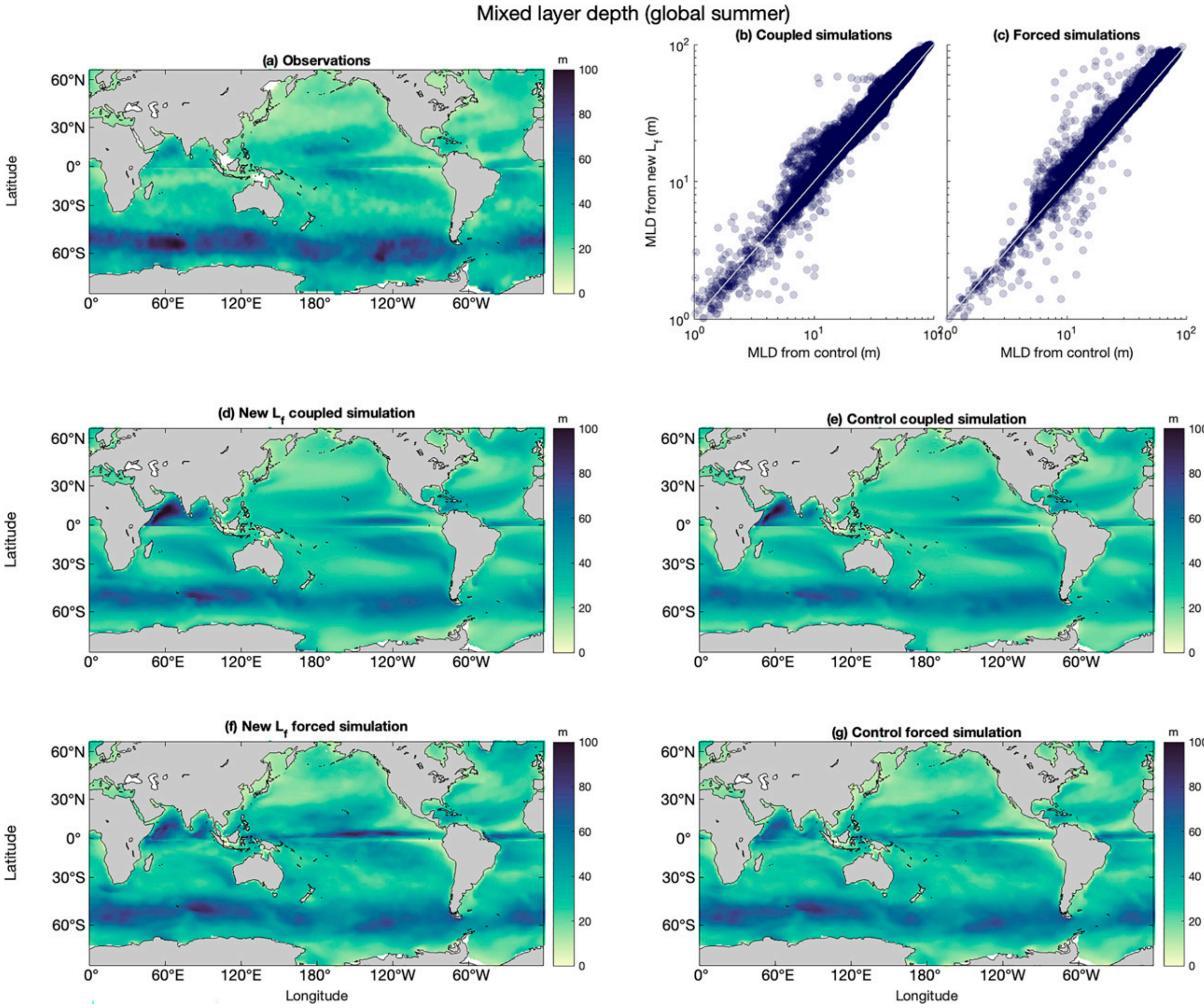

FIG. 5. Global maps of mean mixed layer depth during summer in the Northern Hemisphere (July–September) and Southern Hemisphere (January–March) from (a) observations given by the de Boyer Montégut et al. (2004) dataset updated to include Argo data up to 2012, (b),(c) MLD given by new L_f vs control in all simulations and over all grid points; (d),(e) corresponding global maps in the coupled simulations and (f),(g) forced simulations.

TTW balance. The new frontal width scaling utilizes variables from boundary layer turbulence schemes u_*, w_*, and h, which are readily available in climate models. The need for an artificial frictional time scale parameter τ, which was designed to prevent singularities near the equator in the previous version is eliminated, and it avoids the dependence on boundary layer buoyancy frequency N, which is not reliable in GCMs. As argued throughout this article, the boundary layer turbulence varies widely under forcing, so using a fixed time scale in Fox-Kemper et al. (2011) was not justified. In considering the broader behavior of boundary layer turbulence, where both the frontal scale and other turbulence statistics differ, this artificial factor is just not needed for the scaling and equatorial behavior is more trustworthy.

The new scaling also depends on the local Rossby, Ekman, and turbulent Richardson numbers. Several physical assumptions were made to reduce the number of dependent variables, of which the Rossby and Ekman numbers are assumed to be 1, as expected for the submesoscale. The Richardson number is set to 0.25, representing the arrest by horizontal shear instability.

We test this new scaling over a variety of turbulent processes resulting from winds, waves, and convection that lead to arrested submesoscale fronts and filaments in LES. The predicted frontal width from the new scaling is found be in the same order of the measured frontal width for all cases. Additionally, boundary layer data from the GOTM over four active submesoscale regions was used to estimate the possible range for the new frontal width scaling, which was found to be qualitatively consistent with the submesoscale range of $O(1)$ km. Global estimates of the new scaling were found using a unique configuration of the submesoscale-permitting MITgcm-LLC4320 in tandem with GOTM from Dong et al.

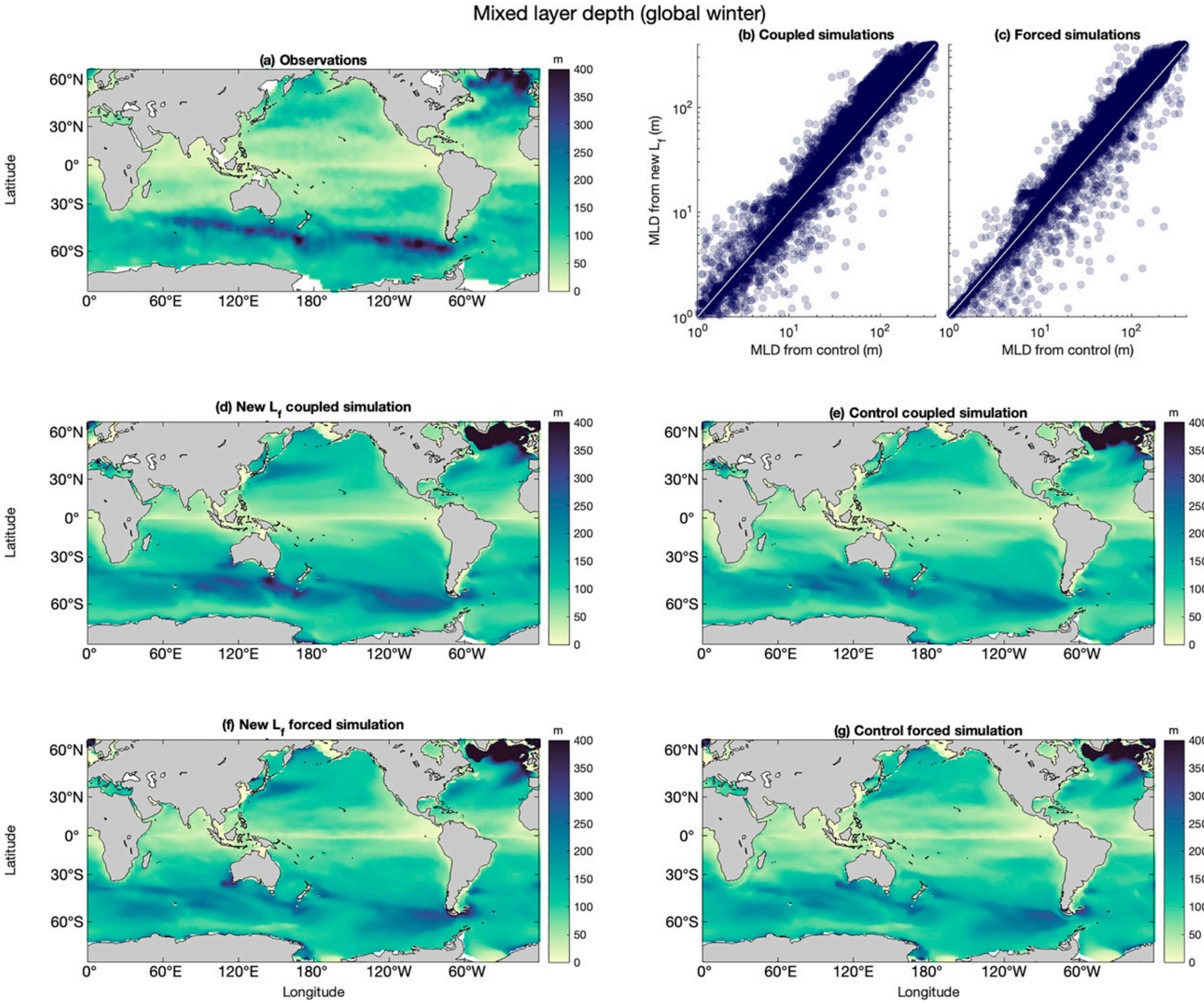

FIG. 6. As in Fig. 5, but during winter in the Northern Hemisphere (January–March) and Southern Hemisphere (July–September).

(2020), which displayed fronts as sharp as 10 m and up to roughly 50 km near the equator. An exciting future prospect is continuing to evaluate the scaling in observed fronts, perhaps even from satellite datasets (e.g., Ullman et al. 2007; Rascle et al. 2020).

The new scaling for frontal width is implemented in the MLE parameterization and tested in forced and coupled CESM2.1.3-POP simulations, where climate sensitivity was primarily estimated through the impact on the mixed layer depth. Since the new parameterization depends on surface forcing, there is merit in both types of simulations: the coupled simulations have active feedback with the atmosphere, which come back through u_* and w_* by changing mixed layer depth and sea surface temperature. The forced simulations are useful for model-observation comparison, as they are forced by observational measurements. However, the CORE-v2 dataset used here is inferior to the newer JRA55-do dataset that has recently been shown to reduce bias in mixed layer depth (Tsujino et al. 2020). Thus, future work will also include testing the new MLE parameterization in a JRA55-do forced simulation for a more robust comparison with observations.

The MLE streamfunction is stronger for sharper fronts, that is, for smaller L_f. The frontal width range found by the GOTM and MITgcm-LLC4320 data demonstrates that the new scaling is able to arrive at smaller L_f than predicted by the previous scaling, consistent with the amazingly sharp fronts observed. This will enhance the restratification effect, which is especially important in regions where there is still a bias toward deeper mixed layer depths (e.g., near the equator in summertime).

The LES analysis has demonstrated how important forcing effects such as Langmuir turbulence corrections and penetrating solar corrections are, so adjustments already made in boundary layer schemes, such as a wave-driven turbulence enhancement factor, are readily adapted. This enhancement factor is also available in turbulent mixing schemes in CESM, and future work will include incorporating the effects of Langmuir turbulence in the MLE parameterization. It can be expected that the contribution of Langmuir turbulence will be

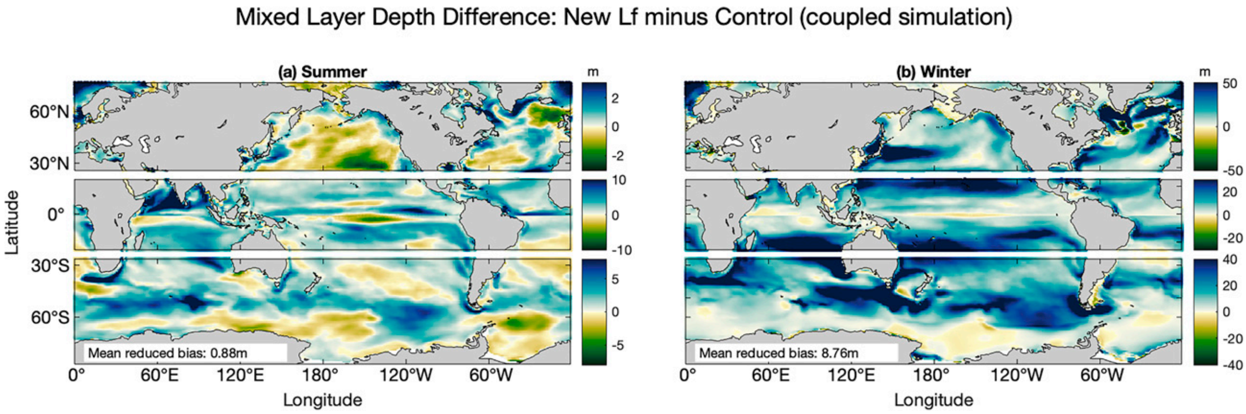

FIG. 7. Differences between the mixed layer depth given from the new L_f and control in the coupled simulations during summer and winter in both hemispheres, as in Fig. 5. Note the different color bars to emphasize regional variability. Positive and negative values relate to MLD deepening and shoaling, respectively. The mean reduced bias is given for each season by the average of the $\mathrm{RMSE}_{\text{new-}L_f} - \mathrm{RMSE}_{\text{control}}$, where RMSE is the root-mean-square error of each case relative to observations.

most significant in the Southern Ocean, where waves tend to be large (Young 1994; Belcher et al. 2012).

Dong et al. (2020, 2021) estimate the scale of symmetric and mixed layer instabilities globally, yet on a local scale it is presently unclear if one dominates over the other and if one is more likely to occur if both conditions are favorable. The Richardson number parameter in the new frontal width scaling is representative of the arrest mechanism. If the front is arrested before reaching horizontal shear instability, the Richardson number could be on order 1 or larger, which may result in frontal widths much larger than currently predicted. Furthermore, if symmetric instability is an important arrest mechanism, it is expected that the MLE parameterization commute with the symmetric instability parameterization and mixing properties given by Bachman et al. (2017).

The new scaling for frontal width was tested using LES of arrested filament frontogenesis, which was treated as two separate fronts for the purposes here. However, the dynamics of filaments have been shown to be different in several aspects, especially in the presence of winds and waves (e.g., Suzuki et al. 2016; Sullivan and McWilliams 2018, 2019). The current MLE parameterization represents the restratifying process of a slumping front, yet MLE may also form along submesoscale filaments if there is sufficient available potential energy stored in the vertical isopycnals. How significant this is, how likely this occurs in nature, and whether the MLE parameterization needs to be modified to include these effects is left for future work.

Frontogenesis is ubiquitous at the submesoscale in the surface layer, whether because of direct action on mesoscale surface horizontal buoyancy gradients or as a secondary frontogenesis in mixed layer eddies that originate from surface-layer baroclinic instability, and whether due to the ambient strain rate or TTW. The end state of frontogenesis is frontal arrest at a finite scale, usually with large Reynolds number, followed by frontal decay. In this paper we propose scaling estimates for the horizontal scale of frontal arrest L_f and the eddy-induced streamfunction Ψ that are expressed entirely in terms of coarse-grid quantities available in climate models. The premises of the proposal are twofold: 1) arrest involves frontal instabilities of various types that limit the horizontal and vertical shear of the front to $O(1)$ bulk values of Ro and

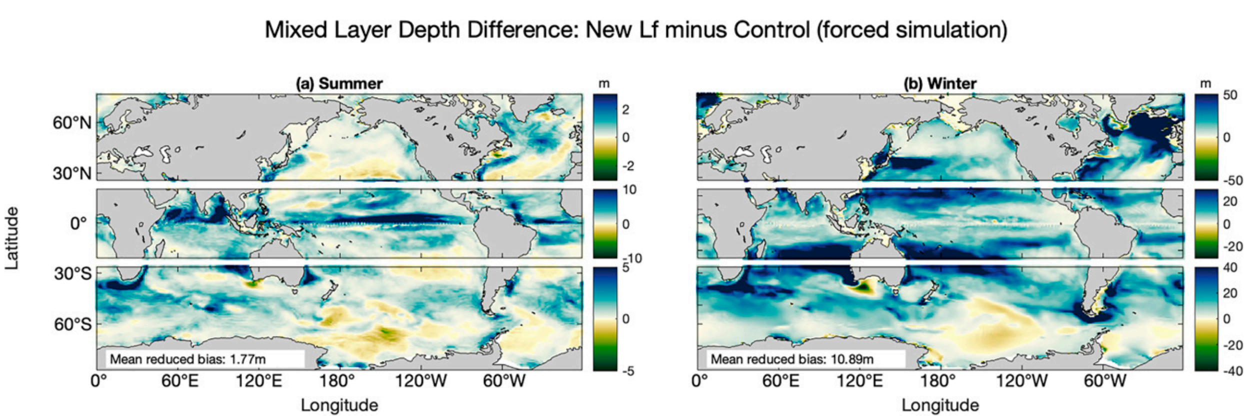

FIG. 8. As in Fig. 7, but for the forced simulations.

Ri, and 2) boundary layer-turbulence on scales smaller than the front are usually involved in the arrest, leading to an $O(1)$ value of Ek (as in the classical Ekman model with $h \sim \sqrt{\nu/f}$, mean current $U \sim u_*^2/fh$, and $\nu \sim u_* h$). The implicated coarse-grid quantities are $\Delta s \nabla_H \overline{b}^z \sim \Delta b$ on the grid scale, f and h from the surface-layer stratification, and (u_*, w_*) from the surface fluxes. The proposed scaling relations (24) and (27) are not inconsistent with the available LES simulations, although as yet only an unsystematic and limited survey of Ro, Ri, and Ek values is available. Much still remains to be learned about the fluid mechanics of how frontal instabilities, frontally enhanced boundary layer turbulence and boundary-forced turbulence interactions with fronts behave during arrest.

This study intends to demonstrate plausibility, and a proper parameter analysis needs to be performed in order to evaluate the parameterization with simulations that are specifically designed for it. As shown in the supplemental material, fronts can also be arrested by other type of turbulence not captured in the TTW framework (e.g., smaller MLEs without surface forcing). Furthermore, the stress imposed by wind effects can either lead to sharpening or spreading of the front depending on the wind direction, which is not accounted for in this framework. A more comprehensive parameter search is needed to evaluate and compare our results with other scalings for frontal widths under different regimes (e.g., Mahadevan et al. 2010; Wenegrat et al. 2018; Crowe and Taylor 2020). Furthermore, turbulent dissipation rate and frontal width are often a measured observational product. Comparing a wide set of fronts of different sizes, dissipation and surface forcing may help support or counter this scaling.

From CESM3 on, CESM will primarily include the Modular Ocean Model (MOM6). This model includes the ePBL mixing scheme, which allows the use of the precise values of m_* and n_* in the frontal width scaling, as well as the standard u_*, w_*, and h as in the current KPP-based version. The factor $(m_* u_*^3 + n_* w_*^3)^{2/3}$ can thus be directly extracted from ePBL or ePBL-LT [to include the enhancement factor due to Langmuir turbulence (LT)]. Including these parameterizations will be an improvement on the current version implemented here, which only uses the average values of m_* and n_* from Reichl and Hallberg (2018). The boundary layer depth h is proportional to u_* and w_*, thus the limit $u_*, w_* \to 0$ is assumed to be stable as h also becomes small. However, additional testing is ongoing to determine whether some averaging is appropriate to avoid momentary instances when $u_*, w_* = 0$, which may lead to singularities in Ψ.

In the limit that $f \to 0$ the new scaling predicts that L_f becomes increasingly large. This limit is also analogous to the case of a truly nonrotating front (e.g., dam break, Özgökmen et al. 2007), where there is no steady frontal width, as geostrophic balance and thermal wind balance do not constrain the result to remain finite. Thus, $\Delta s/L_f \to 0$ as the equator is approached, which means that the parameterization shuts itself off as the MLE scale becomes resolved (e.g., Dong et al. 2020). Furthermore, climate models often refine their grid as to resolve tropical instability waves, which resemble MLI in energy source and vertical location (e.g., Danabasoglu et al. 2012), and thus an MLE parameterization active together with resolved mixed layer instabilities would lead to erroneous and nonphysical estimates.

Estimating changes in the mixed layer depth due to the new MLE parameterization gives the most direct impact on climate sensitivity (e.g., Tsujino et al. 2020; Hall and Fox-Kemper 2021, manuscript submitted to *Geophys. Res. Lett.*). However, there are several other metrics of significant broader climatic impacts that should be evaluated. These include air–sea fluxes and gas exchanges such as CFCs for the impact on the biogeochemical cycle, surface and subsurface tracers such as temperature and salinity, "ideal age" for the effect on ventilation pathways of different water masses below the mixed layer, and on the global scale through the meridional overturning circulation, deep water formation, and average global temperatures. A more comprehensive study is in planning for a more complete application, where model bias and sensitivity are compared with observations in a multimodel multiresolution experiment that may include coupled and JRA55-do forced simulations from CESM-MOM6, CESM-POP, and GFDL-MOM6. Efforts to implement new versions of the MLE parameterization in MOM6 and other models are ongoing.

Acknowledgments. ASB, PSH, and BFK's research was made possible in part by a grant from The Gulf of Mexico Research Initiative, and in part by ONR N00014-17-1-2963. LJ, BFK, and PSH were also supported by ONR N00014-17-1-2393. Conversations with Qing Li, Stephen Griffies, and Alistair Adcroft are happily acknowledged as improving this manuscript.

Data availability statement. Data and code used in the production of this work are available at https://doi.org/10.26300/sf8w-0045.

REFERENCES

Bachman, S., and B. Fox-Kemper, 2013: Eddy parameterization challenge suite I: Eady spindown. *Ocean Modell.*, **64**, 12–28, https://doi.org/10.1016/j.ocemod.2012.12.003.

——, ——, and F. O. Bryan, 2015: A tracer-based inversion method for diagnosing eddy-induced diffusivity and advection. *Ocean Modell.*, **86**, 1–14, https://doi.org/10.1016/j.ocemod.2014.11.006.

——, ——, J. R. Taylor, and L. N. Thomas, 2017: Parameterization of frontal symmetric instabilities. I: Theory for resolved fronts. *Ocean Modell.*, **109**, 72–95, https://doi.org/10.1016/j.ocemod.2016.12.003.

Belcher, S. E., and Coauthors, 2012: A global perspective on Langmuir turbulence in the ocean surface boundary layer. *Geophys. Res. Lett.*, **39**, L18605, https://doi.org/10.1029/2012GL052932.

Boccaletti, G., R. Ferrari, and B. Fox-Kemper, 2007: Mixed layer instabilities and restratification. *J. Phys. Oceanogr.*, **37**, 2228–2250, https://doi.org/10.1175/JPO3101.1.

Bodner, A. S., and B. Fox-Kemper, 2020: A breakdown in potential vorticity estimation delineates the submesoscale-to-turbulence boundary in large eddy simulations. *J. Adv. Model. Earth Syst.*, **12**, e2020MS002049, https://doi.org/10.1029/2020MS002049.

——, ——, L. P. Van Roekel, J. C. McWilliams, and P. P. Sullivan, 2020: A perturbation approach to understanding the effects of turbulence on frontogenesis. *J. Fluid Mech.*, **883**, A25, https://doi.org/10.1017/jfm.2019.804.

Callies, J., and R. Ferrari, 2018a: Baroclinic instability in the presence of convection. *J. Phys. Oceanogr.*, **48**, 45–60, https://doi.org/10.1175/JPO-D-17-0028.1.

——, and ——, 2018b: Note on the rate of restratification in the baroclinic spindown of fronts. *J. Phys. Oceanogr.*, **48**, 1543–1553, https://doi.org/10.1175/JPO-D-17-0175.1.

Calvert, D., G. Nurser, M. J. Bell, and B. Fox-Kemper, 2020: The impact of a parameterisation of submesoscale mixed layer eddies on mixed layer depths in the NEMO ocean model. *Ocean Modell.*, **154**, 101678, https://doi.org/10.1016/j.ocemod.2020.101678.

Capet, X., J. C. McWilliams, M. J. Molemaker, and A. F. Shchepetkin, 2008: Mesoscale to submesoscale transition in the California Current System. Part I: Flow structure, eddy flux, and observational tests. *J. Phys. Oceanogr.*, **38**, 29–43, https://doi.org/10.1175/2007JPO3671.1.

Cronin, M. F., and W. S. Kessler, 2009: Near-surface shear flow in the tropical Pacific cold tongue front. *J. Phys. Oceanogr.*, **39**, 1200–1215, https://doi.org/10.1175/2008JPO4064.1.

Crowe, M., and J. R. Taylor, 2020: The effects of surface wind stress and buoyancy flux on the evolution of a front in a turbulent thermal wind balance. *Fluids*, **5**, 87, https://doi.org/10.3390/fluids5020087.

Dale, A. C., J. A. Barth, M. D. Levine, and J. A. Austin, 2008: Observations of mixed layer restratification by onshore surface transport following wind reversal in a coastal upwelling region. *J. Geophys. Res.*, **113**, C01010, https://doi.org/10.1029/2007JC004128.

Danabasoglu, G., S. C. Bates, B. P. Briegleb, S. R. Jayne, M. Jochum, W. G. Large, S. Peacock, and S. G. Yeager, 2012: The CCSM4 ocean component. *J. Climate*, **25**, 1361–1389, https://doi.org/10.1175/JCLI-D-11-00091.1.

Dauhajre, D. P., and J. C. McWilliams, 2018: Diurnal evolution of submesoscale front and filament circulations. *J. Phys. Oceanogr.*, **48**, 2343–2361, https://doi.org/10.1175/JPO-D-18-0143.1.

de Boyer Montégut, C., G. Madec, A. S. Fischer, A. Lazar, and D. Iudicone, 2004: Mixed layer depth over the global ocean: An examination of profile data and a profile-based climatology. *J. Geophys. Res.*, **109**, C12003, https://doi.org/10.1029/2004JC002378.

Dong, J., B. Fox-Kemper, H. Zhang, and C. Dong, 2020: The scale of submesoscale baroclinic instability globally. *J. Phys. Oceanogr.*, **50**, 2649–2667, https://doi.org/10.1175/JPO-D-20-0043.1.

——, ——, ——, and ——, 2021: The scale and activity of symmetric instability estimated from a global submesoscale-permitting ocean model. *J. Phys. Oceanogr.*, **51**, 1655–1670, https://doi.org/10.1175/JPO-D-20-0159.1.

Fox-Kemper, B., R. Ferrari, and R. Hallberg, 2008: Parameterization of mixed layer eddies. Part I: Theory and diagnosis. *J. Phys. Oceanogr.*, **38**, 1145–1165, https://doi.org/10.1175/2007JPO3792.1.

——, and Coauthors, 2011: Parameterization of mixed layer eddies. III: Implementation and impact in global ocean climate simulations. *Ocean Modell.*, **39**, 61–78, https://doi.org/10.1016/j.ocemod.2010.09.002.

——, and Coauthors, 2019: Challenges and prospects in ocean circulation models. *Front. Mar. Sci.*, **6**, 65, https://doi.org/10.3389/fmars.2019.00065.

——, L. Johnson, and F. Qiao, 2022: Ocean near-surface layers. *Ocean Mixing*, M. Meredith and A. Naveira Garabato, Eds., Elsevier, 65–94.

Garrett, C. J. R., and J. W. Loder, 1981: Dynamical aspects of shallow sea fronts. *Philos. Trans. Roy. Soc.*, **A302**, 563–581, https://doi.org/10.1098/rsta.1981.0183.

Gent, P. R., and J. C. McWilliams, 1990: Isopycnal mixing in ocean circulation models. *J. Phys. Oceanogr.*, **20**, 150–155, https://doi.org/10.1175/1520-0485(1990)020<0150:IMIOCM>2.0.CO;2.

——, ——, and C. Snyder, 1994: Scaling analysis of curved fronts. Validity of the balance equations and semigeostrophy. *J. Atmos. Sci.*, **51**, 160–163, https://doi.org/10.1175/1520-0469(1994)051<0160:SAOCFV>2.0.CO;2.

Grant, A. L. M., and S. E. Belcher, 2009: Characteristics of Langmuir turbulence in the ocean mixed layer. *J. Phys. Oceanogr.*, **39**, 1871–1887, https://doi.org/10.1175/2009JPO4119.1.

Griffies, S. M., 1998: The Gent–McWilliams skew flux. *J. Phys. Oceanogr.*, **28**, 831–841, https://doi.org/10.1175/1520-0485(1998)028<0831:TGMSF>2.0.CO;2.

Gula, J., M. J. Molemaker, and J. C. McWilliams, 2014: Submesoscale cold filaments in the gulf stream. *J. Phys. Oceanogr.*, **44**, 2617–2643, https://doi.org/10.1175/JPO-D-14-0029.1.

——, ——, and ——, 2016: Topographic generation of submesoscale centrifugal instability and energy dissipation. *Nat. Commun.*, **7**, 12811, https://doi.org/10.1038/ncomms12811.

Haine, T. W. N., and J. Marshall, 1998: Gravitational, symmetric, and baroclinic instability of the ocean mixed layer. *J. Phys. Oceanogr.*, **28**, 634–658, https://doi.org/10.1175/1520-0485(1998)028<0634:GSABIO>2.0.CO;2.

Hamlington, P. E., L. P. Van Roekel, B. Fox-Kemper, K. Julien, and G. P. Chini, 2014: Langmuir–submesoscale interactions: Descriptive analysis of multiscale frontal spindown simulations. *J. Phys. Oceanogr.*, **44**, 2249–2272, https://doi.org/10.1175/JPO-D-13-0139.1.

Haney, S., B. Fox-Kemper, K. Julien, and A. Webb, 2015: Symmetric and geostrophic instabilities in the wave-forced ocean mixed layer. *J. Phys. Oceanogr.*, **45**, 3033–3056, https://doi.org/10.1175/JPO-D-15-0044.1.

Hosegood, P., M. C. Gregg, and M. H. Alford, 2006: Submesoscale lateral density structure in the oceanic surface mixed layer. *Geophys. Res. Lett.*, **33**, L22604, https://doi.org/10.1029/2006GL026797.

Hoskins, B. J., 1974: The role of potential vorticity in symmetric stability and instability. *Quart. J. Roy. Meteor. Soc.*, **100**, 480–482, https://doi.org/10.1002/qj.49710042520.

——, and F. P. Bretherton, 1972: Atmospheric frontogenesis models: Mathematical formulation and solution. *J. Atmos. Sci.*, **29**, 11–37, https://doi.org/10.1175/1520-0469(1972)029<0011:AFMMFA>2.0.CO;2.

Johnson, L., C. M. Lee, E. A. D'Asaro, L. Thomas, and A. Shcherbina, 2020: Restratification at a California current upwelling front. Part I: Observations. *J. Phys. Oceanogr.*, **50**, 1455–1472, https://doi.org/10.1175/JPO-D-19-0203.1.

Kraus, E. B., and J. S. Turner, 1967: A one-dimensional model of the seasonal thermocline II. The general theory and its consequences. *Tellus*, **19**, 98–106, https://doi.org/10.3402/tellusa.v19i1.9753.

Large, W. G., and S. G. Yeager, 2009: The global climatology of an interannually varying air–sea flux data set. *Climate Dyn.*, **33**, 341–364, https://doi.org/10.1007/s00382-008-0441-3.

——, J. C. McWilliams, and S. C. Doney, 1994: Oceanic vertical mixing: A review and a model with a nonlocal boundary layer parameterization. *Rev. Geophys.*, **32**, 363–403, https://doi.org/10.1029/94RG01872.

Levy, M., G. Danabasoglu, S. Griffies, T. Ringler, A. Adcroft, R. Hallberg, D. Jacobsen, and W. Large, 2014: Community ocean vertical mixing (CVMix) parameterizations. *Ocean Model Working Group Meeting*, Boulder, CO, UCAR, https://www.cesm.ucar.edu/events/wg-meetings/2014/presentations/omwg/levy.pdf.

Lévy, M., P. J. S. Franks, and K. S. Smith, 2018: The role of submesoscale currents in structuring marine ecosystems. *Nat. Commun.*, **9**, 4758, https://doi.org/10.1038/s41467-018-07059-3.

Li, Q., and B. Fox-Kemper, 2017: Assessing the effects of Langmuir turbulence on the entrainment buoyancy flux in the ocean surface boundary layer. *J. Phys. Oceanogr.*, **47**, 2863–2886, https://doi.org/10.1175/JPO-D-17-0085.1.

——, and Coauthors, 2019: Comparing ocean surface boundary vertical mixing schemes including Langmuir turbulence. *J. Adv. Model. Earth Syst.*, **11**, 3545–3592, https://doi.org/10.1029/2019MS001810.

——, J. Bruggeman, H. Burchard, K. Klingbeil, L. Umlauf, and K. Bolding, 2021: Integrating CVMIX into GOTM (v6. 0): A consistent framework for testing, comparing, and applying ocean mixing schemes. *Geosci. Model Dev.*, **14**, 4261–4282, https://doi.org/10.5194/gmd-14-4261-2021.

Lucas, A. J., and Coauthors, 2016: Adrift upon a salinity-stratified sea: A view of upper-ocean processes in the bay of bengal during the southwest monsoon. *Oceanography*, **29**, 134–145, https://doi.org/10.5670/oceanog.2016.46.

Mahadevan, A., 2016: The impact of submesoscale physics on primary productivity of plankton. *Annu. Rev. Mar. Sci.*, **8**, 161–184, https://doi.org/10.1146/annurev-marine-010814-015912.

——, A. Tandon, and R. Ferrari, 2010: Rapid changes in mixed layer stratification driven by submesoscale instabilities and winds. *J. Geophys. Res.*, **115**, C03017, https://doi.org/10.1029/2008JC005203.

McWilliams, J. C., 2016: Submesoscale currents in the ocean. *Proc. Roy. Soc.*, **472A**, 20160117, https://doi.org/10.1098/rspa.2016.0117.

——, 2017: Submesoscale surface fronts and filaments: Secondary circulation, buoyancy flux, and frontogenesis. *J. Fluid Mech.*, **823**, 391–432, https://doi.org/10.1017/jfm.2017.294.

——, 2021: Oceanic frontogenesis. *Annu. Rev. Mar. Sci.*, **13**, 227–253, https://doi.org/10.1146/annurev-marine-032320-120725.

——, and J. M. Molemaker, 2011: Baroclinic frontal arrest: A sequel to unstable frontogenesis. *J. Phys. Oceanogr.*, **41**, 601–619, https://doi.org/10.1175/2010JPO4493.1.

——, P. P. Sullivan, and C.-H. Moeng, 1997: Langmuir turbulence in the ocean. *J. Fluid Mech.*, **334**, 1–30, https://doi.org/10.1017/S0022112096004375.

——, M. J. Molemaker, and E. I. Olafsdottir, 2009: Linear fluctuation growth during frontogenesis. *J. Phys. Oceanogr.*, **39**, 3111–3129, https://doi.org/10.1175/2009JPO4186.1.

——, J. Gula, J. M. Molemaker, L. Renault, and A. F. Shchepetkin, 2015: Filament frontogenesis by boundary layer turbulence. *J. Phys. Oceanogr.*, **45**, 1988–2005, https://doi.org/10.1175/JPO-D-14-0211.1.

Mironov, D., A. Terzhevik, G. Kirillin, T. Jonas, J. Malm, and D. Farmer, 2002: Radiatively driven convection in ice-covered lakes: Observations, scaling, and a mixed layer model. *J. Geophys. Res.*, **107**, 3032, https://doi.org/10.1029/2001JC000892.

Nagai, T., A. Tandon, and D. L. Rudnick, 2006: Two-dimensional ageostrophic secondary circulation at ocean fronts due to vertical mixing and large-scale deformation. *J. Geophys. Res.*, **111**, C09038, https://doi.org/10.1029/2005JC002964.

Nurser, A. J. G., and J. W. Zhang, 2000: Eddy-induced mixed layer shallowing and mixed layer/thermocline exchange. *J. Geophys. Res.*, **105**, 21 851–21 868, https://doi.org/10.1029/2000JC900018.

Olita, A., and Coauthors, 2017: Frontal dynamics boost primary production in the summer stratified mediterranean sea. *Ocean Dyn.*, **67**, 767–782, https://doi.org/10.1007/s10236-017-1058-z.

Özgökmen, T. M., T. Iliescu, P. F. Fischer, A. Srinivasan, and J. Duan, 2007: Large eddy simulation of stratified mixing in two-dimensional dam-break problem in a rectangular enclosed domain. *Ocean Modell.*, **16**, 106–140, https://doi.org/10.1016/j.ocemod.2006.08.006.

Pallàs-Sanz, E., T. M. S. Johnston, and D. L. Rudnick, 2010: Frontal dynamics in a California current system shallow front: 1. Frontal processes and tracer structure. *J. Geophys. Res.*, **115**, C12067, https://doi.org/10.1029/2009JC006032.

Price, J. F., R. A. Weller, and R. Pinkel, 1986: Diurnal cycling: Observations and models of the upper ocean response to diurnal heating, cooling, and wind mixing. *J. Geophys. Res.*, **91**, 8411–8427, https://doi.org/10.1029/JC091iC07p08411.

Ramachandran, S., and Coauthors, 2018: Submesoscale processes at shallow salinity fronts in the Bay of Bengal: Observations during the winter monsoon. *J. Phys. Oceanogr.*, **48**, 479–509, https://doi.org/10.1175/JPO-D-16-0283.1.

Rascle, N., and Coauthors, 2020: Monitoring intense oceanic fronts using sea surface roughness: Satellite, airplane, and in situ comparison. *J. Geophys. Res. Oceans*, **125**, e2019JC015704, https://doi.org/10.1029/2019JC015704.

Reichl, B. G., and R. Hallberg, 2018: A simplified energetics based planetary boundary layer (ePBL) approach for ocean climate simulations. *Ocean Modell.*, **132**, 112–129, https://doi.org/10.1016/j.ocemod.2018.10.004.

Rocha, C. B., T. K. Chereskin, S. T. Gille, and D. Menemenlis, 2016: Mesoscale to submesoscale wavenumber spectra in Drake Passage. *J. Phys. Oceanogr.*, **46**, 601–620, https://doi.org/10.1175/JPO-D-15-0087.1.

Rotunno, R., W. C. Skamarock, and C. Snyder, 1994: An analysis of frontogenesis in numerical simulations of baroclinic waves. *J. Atmos. Sci.*, **51**, 3373–3398, https://doi.org/10.1175/1520-0469(1994)051<3373:AAOFIN>2.0.CO;2.

Skyllingstad, E. D., and R. Samelson, 2012: Baroclinic frontal instabilities and turbulent mixing in the surface boundary layer. Part I: Unforced simulations. *J. Phys. Oceanogr.*, **42**, 1701–1716, https://doi.org/10.1175/JPO-D-10-05016.1.

Smith, K. M., P. E. Hamlington, and B. Fox-Kemper, 2016: Effects of submesoscale turbulence on ocean tracers. *J. Geophys. Res. Oceans*, **121**, 908–933, https://doi.org/10.1002/2015JC011089.

Su, Z., J. Wang, P. Klein, A. F. Thompson, and D. Menemenlis, 2018: Ocean submesoscales as a key component of the global heat budget. *Nat. Commun.*, **9**, 775, https://doi.org/10.1038/s41467-018-02983-w.

Sullivan, P. P., and J. C. McWilliams, 2018: Frontogenesis and frontal arrest of a dense filament in the oceanic surface boundary layer. *J. Fluid Mech.*, **837**, 341–380, https://doi.org/10.1017/jfm.2017.833.

——, and ——, 2019: Langmuir turbulence and filament frontogenesis in the oceanic surface boundary layer. *J. Fluid Mech.*, **879**, 512–553, https://doi.org/10.1017/jfm.2019.655.

——, ——, and W. K. Melville, 2007: Surface gravity wave effects in the oceanic boundary layer: Large-eddy simulation with vortex force and stochastic breakers. *J. Fluid Mech.*, **593**, 405–452, https://doi.org/10.1017/S002211200700897X.

Suzuki, N., B. Fox-Kemper, P. E. Hamlington, and L. P. Van Roekel, 2016: Surface waves affect frontogenesis. *J. Geophys. Res. Oceans*, **121**, 3597–3624, https://doi.org/10.1002/2015JC011563.

Tandon, A., and C. Garrett, 1994: Mixed layer restratification due to a horizontal density gradient. *J. Phys. Oceanogr.*, **24**, 1419–1424, https://doi.org/10.1175/1520-0485(1994)024<1419:MLRDTA>2.0.CO;2.

Taylor, J. R., and R. Ferrari, 2011: Ocean fronts trigger high latitude phytoplankton blooms. *Geophys. Res. Lett.*, **38**, L23601, https://doi.org/10.1029/2011GL049312.

Teixeira, M. C., and S. E. Belcher, 2002: On the distortion of turbulence by a progressive surface wave. *J. Fluid Mech.*, **458**, 229–267, https://doi.org/10.1017/S0022112002007838.

Thomas, L. N., J. R. Taylor, R. Ferrari, and T. M. Joyce, 2013: Symmetric instability in the gulf stream. *Deep-Sea Res. II*, **91**, 96–110, https://doi.org/10.1016/j.dsr2.2013.02.025.

Thompson, A. F., A. Lazar, C. Buckingham, A. C. Naveira Garabato, G. M. Damerell, and K. J. Heywood, 2016: Open-ocean submesoscale motions: A full seasonal cycle of mixed layer instabilities from gliders. *J. Phys. Oceanogr.*, **46**, 1285–1307, https://doi.org/10.1175/JPO-D-15-0170.1.

Thompson, L., 2000: Ekman layers and two-dimensional frontogenesis in the upper ocean. *J. Geophys. Res.*, **105**, 6437–6451, https://doi.org/10.1029/1999JC900336.

Thorpe, S. A., 2005: *The Turbulent Ocean.* Cambridge University Press, 496 pp.

Timmermans, M.-L., and P. Winsor, 2013: Scales of horizontal density structure in the Chukchi Sea surface layer. *Cont. Shelf Res.*, **52**, 39–45, https://doi.org/10.1016/j.csr.2012.10.015.

Tsujino, H., and Coauthors, 2020: Evaluation of global ocean–sea-ice model simulations based on the experimental protocols of the Ocean Model Intercomparison Project phase 2 (OMIP-2). *Geosci. Model Dev.*, **13**, 3643–3708, https://doi.org/10.5194/gmd-13-3643-2020.

Ullman, D. S., P. C. Cornillon, and Z. Shan, 2007: On the characteristics of subtropical fronts in the North Atlantic. *J. Geophys. Res.*, **112**, C01010, https://doi.org/10.1029/2006JC003601.

Umlauf, L., and H. Burchard, 2005: Second-order turbulence closure models for geophysical boundary layers. A review of recent work. *Cont. Shelf Res.*, **25**, 795–827, https://doi.org/10.1016/j.csr.2004.08.004.

Van Roekel, L. P., P. E. Hamlington, and B. Fox-Kemper, 2012: Multiscale simulations of Langmuir cells and submesoscale eddies using XSEDE resources. *Proc. XSEDE12 First Conf. of the Extreme Science and Engineering Discovery Environment*, Chicago, IL, ACM, 20, https://doi.org/10.1145/2335755.2335816.

——, and Coauthors, 2018: The KPP boundary layer scheme for the ocean: Revisiting its formulation and benchmarking one-dimensional simulations relative to LES. *J. Adv. Model. Earth Syst.*, **10**, 2647–2685, https://doi.org/10.1029/2018MS001336.

Wenegrat, J. O., L. N. Thomas, J. Gula, and J. C. McWilliams, 2018: Effects of the submesoscale on the potential vorticity budget of ocean mode waters. *J. Phys. Oceanogr.*, **48**, 2141–2165, https://doi.org/10.1175/JPO-D-17-0219.1.

Young, I. R., 1994: Global ocean wave statistics obtained from satellite observations. *Appl. Ocean Res.*, **16**, 235–248, https://doi.org/10.1016/0141-1187(94)90023-X.